Constraining uplift and denudation of west African continental margin by inversion of stacking velocity data

H. L. Walford and N. J. White

Bullard Laboratories, Department of Earth Sciences, University of Cambridge, Cambridge, UK

[1]   An inverse model has been developed to determine the magnitude of denudation at seabed and subsurface unconformities by using root-mean-square (RMS) stacking velocity data derived from processing a set of seismic reflection profiles. This approach provides superior spatial coverage in comparison to other methods, such as vitrinite reflectance, apatite fission track, and sonic velocity modeling, which are restricted to borehole locations. The model assumes exponential porosity decay with depth and a standard velocity-porosity relationship in order to compute a synthetic RMS velocity profile. Denudation values at two levels in the stratigraphy are then adjusted until the fit between the model and the data is optimized. Successful modeling is dependent upon independent estimates of the initial porosity of sediment since significant trade-off occurs between initial porosity and denudation. Application to the west African shelf shows that 0.5–1 km of denudation occurred along the entire margin, probably during late Neogene times. The amount of denudation decreases oceanward and was probably triggered by regional tilting associated with initiation and/or regeneration of continent-wide mantle convective upwelling, which is thought to have affected much of subequatorial Africa. A subsurface Oligocene unconformity represents as much as 2.5 km of denudation and was probably produced by initiation of an oceanic current.

Citation: Walford, H. L., and N. J. White (2005), Constraining uplift and denudation of west African continental margin by inversion of stacking velocity data, *J. Geophys. Res.*, *110*, B04403, doi:10.1029/2003JB002893.

1.   Introduction

[2]   Geomorphological observations of Africa, such as the anomalously high topography and unique hypsometry of the continent, have been used by many as evidence of Cenozoic epeirogenic uplift [e.g., *Holmes*, 1965; *Bond*, 1978; *Cogley*, 1985; *Nyblade and Robinson*, 1994; *Burke*, 1996; *Partridge*, 1998]. Seismic tomographic images of the mantle indicate the presence of a slow, and therefore probably hot, region in the lower mantle beneath southern Africa, implying that Africa's epeirogenic uplift may be convectively driven [e.g., *Grand et al.*, 1997; *van der Hilst et al.*, 1997; *Lithgow-Bertelloni and Silver*, 1998; *Ritsema et al.*, 1999; *Gurnis et al.*, 2000; *Zhao*, 2001] (Figure 1). The long-wavelength (>1000 km) free-air gravity anomaly field is positive over much of southern Africa, which further suggests that subplate convection is the driving force for uplift [*Parsons and Daly*, 1983; *McKenzie*, 1994]. This long-wavelength field has been used to estimate the convectively supported part of topography by assuming a value for the admittance, Z, which relates the Fourier transform of topography, h, to that of gravity, g, such that $\bar{g}(k) = Z(k)\bar{h}(k)$. At long wavelengths, admittance is constant and has a value

of 35 mGal km^{-1} within the ocean basins [*Sclater et al.*, 1975; *McKenzie*, 1994]. In continental regions, the admittance increases to 50 mGal km^{-1}. Thus convective support of topography, h_{conv}, can be isolated by using an estimate of the admittance, since $h_{conv} = g/Z$ where g is the long-wavelength free-air gravity anomaly (Figure 1) [*McKenzie*, 1994].

[3]   In order to test the hypothesis that mantle convection has played and continues to play a significant role in shaping African topography, the uplift history of a continent must be accurately determined over wavelengths of 100–1000 km. Measuring uplift directly is generally not possible since erosion modifies or destroys reference levels. However, by estimating denudation at regional unconformities, the magnitude and distribution of uplift can be inferred. Methods which exploit thermal or mechanical properties of rocks are often used to estimate the amount of material that has been removed at an unconformity but all have important shortcomings. The modeling of thermal markers such as vitrinite reflectance or apatite fission tracks suffers from trade-off between denudation and geothermal history and is dependent upon specific (and usually empirical) parameterizations [e.g., *Brown et al.*, 1990; *Rowley and White*, 1998]. Mechanical methods generally exploit sonic velocity logs but the large scatter typical of such data makes modeling problematical and results are very sensitive to lithological
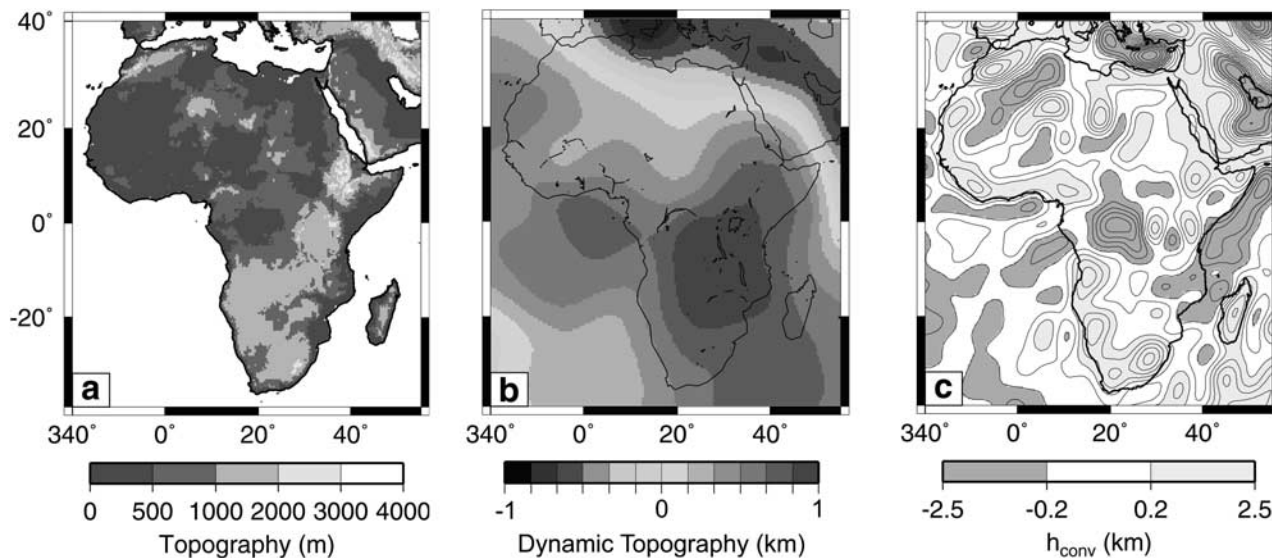
Figure 1. (a) Topography of Africa from ETOPO5 database. (b) Predicted dynamic topography, based on seismic tomography [after *Gurnis et al.*, 2000]. (c) Prediction of convectively supported topography, h_{conv}, based on EGMLM360 free-air gravity anomaly field low-pass filtered at 1000 km (D. McKenzie, personal communication, 2001).

variation [e.g., *Hillis*, 1992, 1995; *Ware and Turner*, 2002]. Cosmogenic nuclides can be used to estimate erosion rates over short geological timescales (typically 10^4–10^5 years), but are of little use over timescales of several million years [e.g., *Gosse and Phillips*, 2001; *Vance et al.*, 2003]. Subsidence analyses of extensional sedimentary basins can be adapted to estimate denudation in basins that have undergone subsequent uplift by comparing the predicted and observed subsidence [e.g., *Rowley and White*, 1998; *Wheeler and White*, 2000; *Jones et al.*, 2001]. This method suffers from the one serious drawback common to all of these approaches: they are limited to borehole locations and thus cannot provide good spatial coverage.

[4] In order to build a three-dimensional picture of the variation in amplitude and distribution of denudation, much better spatial sampling is required. Here, we propose that stacking velocity data obtained during processing of seismic reflection profiles can provide more comprehensive spatial coverage and we show how these data can be modeled to yield estimates of denudation along the West African continental margin. We have chosen this particular margin for three reasons. First, the sedimentary interface between subaerial and submarine realms usually has modest dip and thus is particularly sensitive to regional uplift. Secondly, this margin falls within the influence of the Southern African Superswell and so it is a prime candidate for investigating the relationship between regional epeirogeny and mantle dynamics. Thirdly, the Neogene stratigraphy of this margin comprises thin interbedded sandstones and mudstones whose gross compactional properties are likely to be relatively simple and predictable.

2. Modeling Stacking Velocities on the West African Shelf

[5] A major seabed unconformity occurs offshore West Africa, where Neogene prograding clinoforms have
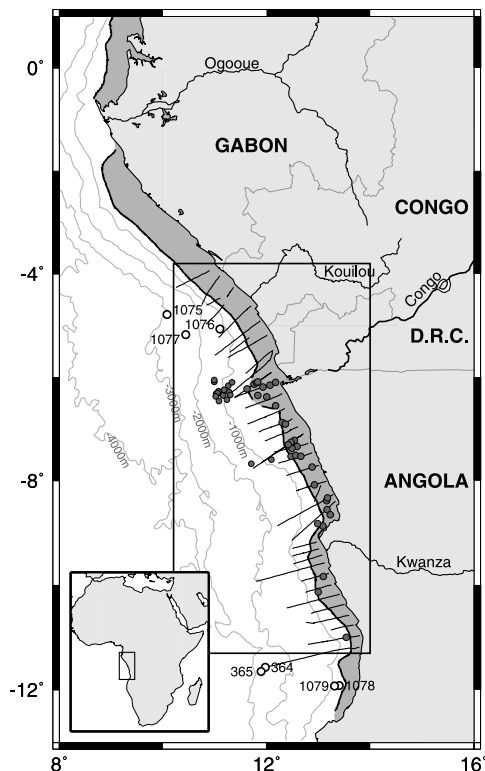

Figure 2. Map of west African continental margin showing extent of seabed unconformity in dark gray. Box indicates region of denudation modeling. Solid lines represent seismic data used for denudation calculations. Gray circles represent wells used to calibrate seismic data. Numbered open circles represent ODP Leg 175 and DSDP sites.
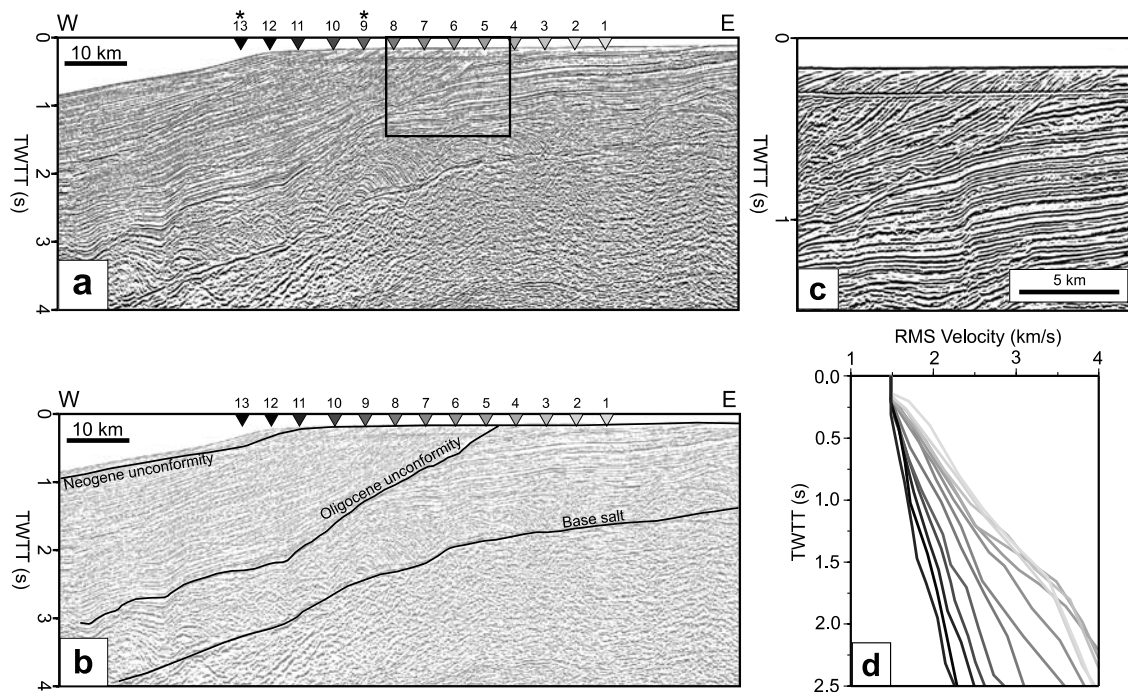
Figure 3. (a) Uninterpreted and (b) interpreted seismic reflection profile, offshore Congo. Triangles represent positions of velocity profiles, asterisks represent V_{RMS} profiles shown in Figure 9. (c) Enlargement of box on Figure 3a, showing unconformity intersecting seabed. (d) V_{RMS} profiles across Congo shelf. Shading corresponds to triangles in Figures 3a and 3b. Note fanning of profiles, velocities get faster toward coast, where denudation is greater. Present-day bathymetry is a consequence of the Holocene marine transgression.

been truncated at the seabed landward of the shelf break (Figures 2 and 3) [*Cramez and Jackson*, 2000]. The youngest sedimentary rocks on the shelf are seen to onlap this unconformity at the edge of the shelf, implying a Pleistocene age (marine isotope stage 12: 0.47–0.44 Ma) for the unconformity [*Uenzelmann-Neben et al.*, 1997; *Uenzelmann-Neben*, 1998]. A second, deeper unconformity has removed much of the Paleogene sediment from the shelf and cuts down into Late Cretaceous rocks (Figure 3) [*Brice et al.*, 1982; *Teisserenc and Villemin*, 1990; *Séranne et al.*, 1992; *Séranne*, 1999; *Cramez and Jackson*, 2000]. Measurements of the thickness of stratigraphy truncated by the subsurface unconformity on depth-converted seismic data suggest that up to 2 km of incision occurred in Oligocene times [*Séranne et al.*, 1992; *Karner et al.*, 1997]. Figure 3 shows incision with an amplitude of approximately 1.1 s two-way travel time. Assuming a sediment velocity of 3 km s^{-1}, this incision is equivalent to ∼1.6 km of denudation.

[6] Quantifying the amount of denudation at the Neogene seabed unconformity is more problematic since this higher level unconformity lacks incisional topography. However, estimates of uplift at this time are important in order to test predictions of regional dynamic uplift [e.g., *Gurnis et al.*, 2000]. Estimates of the magnitude of late Miocene-Pliocene denudation range from 150 m [*Cramez and Jackson*, 2000] to 900 m [*Walgenwitz et al.*, 1990]. *Cramez and Jackson* [2000] base their estimate on observations of Neogene truncation on seismic reflection profiles, but this technique is problematic since it is uncertain where the truncated clinoforms would have 'rolled over' into top sets. However,

it can be stated with some confidence that there was less denudation in the late Neogene than in the Oligocene as the dramatic incision typical of the earlier unconformity is not evident at the seabed. It is unlikely that more than a few hundred meters of sediment have been removed at the seabed. *Walgenwitz et al.* [1990] analyzed fluid inclusions in presalt lithologies offshore Angola to estimate temperatures during Miocene times. The elevated temperatures that they inferred can be explained by a steeper geothermal gradient in Miocene times, by regional flushing of hot fluids, or by a greater depth of burial. Given the stratal geometry of Figure 3a, it seems more likely that denudation has unroofed the margin. Approximately 900 m of sediment must have been removed to account for the observed temperatures.

Table 1. Notation and Values of Model Parameters

Notation	Parameter	Value
D	denudation	
ϕ	porosity	
λ	porosity decay length	
M	residual model misfit	
σ	error in measured velocity	
ρ	bulk rock density	
ρ_{fl}	pore fluid density	1030 kg m^{-3}
ρ_{ma}	grain density	2650 kg m^{-3}
ρ_w	seawater density	1000 kg m^{-3}
t	two-way time	
U	tectonic uplift	
V	velocity	
V_{fl}	pore fluid velocity	1.5 km s^{-1}
V_{ma}	rock matrix velocity	
W	weighting factor	
z	depth	

Table 2. Seismic P Wave Velocity, V_p, and Density of Some Sedimentary Minerals

Mineral	V_p, km s^{-1}	Density, g cm^{-3}	Reference
Quartz	6.05	2.65	*Christensen* [1982]
Muscovite	6.62	2.79	*Christensen* [1982]
Muscovite	5.10	2.79	*Mavko et al.* [1998]
Phlogopite	5.55	2.80	*Christensen* [1982]
Biotite	5.26	3.05	*Christensen* [1982]
Illite	4.32	–	*Mavko et al.* [1998]
Calcite	6.53	2.71	*Christensen* [1982]
Halite	4.55	2.16	*Mavko et al.* [1998]
Anhydrite	5.64	2.98	*Mavko et al.* [1998]
Anhydrite	6.01	2.96	*Mavko et al.* [1998]
Gypsum	5.80	2.35	*Mavko et al.* [1998]

Figure 4. Various velocity-porosity relationships. In all cases, $V_{fl} = 1.5$ km s^{-1} and $V_{ma} = 6$ km s^{-1}.

[7] In a region of uniform lithology, the primary control on seismic velocity is likely to be the porosity of the medium. Porosity is, in turn, controlled by compaction and is therefore a function of the maximum depth of burial. In the case of clastic material, porosity reduction by compaction is largely irreversible and if sediment is later exhumed it will retain the porosity corresponding to its greatest depth of burial. Thus seismic velocity can be used to estimate the amount of denudation that has occurred along the shelf provided that the velocity-depth trend of an unexhumed section is known or can be confidently estimated. We shall ignore the secondary effects of cementation and diagenesis together with complications such as the presence of gas hydrates and hydrocarbons.

[8] Sonic velocity profiles from boreholes are often used to estimate denudation but it is difficult to create a simple model that can account for very short wavelength variation inherent in these data [*Hillis*, 1992, 1995; *Ware and Turner*, 2002]. In contrast, root-mean-square velocity (V_{RMS}) profiles derived from seismic reflection data are, by definition, smooth, since they are an integration of interval velocities over depth [*Yilmaz*, 2001]. This inherent smoothness is a great advantage since it averages out short-wavelength variations caused by lithological variation. Thus V_{RMS} profiles are a potentially useful tool for estimating denudational amplitude. It is clear that V_{RMS} profiles vary systematically across the west African shelf, with velocities decreasing seaward (Figure 3). The thick Cenozoic sedimentary rocks of the west African shelf are dominated by silty mudstones and fine sandstones and there is insufficient lithological variation to account for the observed variation in velocity [*Andersen et al.*, 2000]. Observed velocity changes are most likely caused by porosity variation which arises from denudation at the late Neogene and Oligocene unconformities.

[9] Denudational estimates have been made along the shelf offshore Angola and Congo (Figure 2). Lithostratigraphy and biostratigraphy was available for all wells shown on Figure 2. This area was chosen because it covers a transition from positive to negative long-wavelength gravity anomalies and so may correspond to a change from dynamic uplift to subsidence (Figure 1c). If dynamic topography controls vertical motions of the continent and thus shelfal erosion, there should be a correlation between the intensity of denudation and the distribution of long-wavelength gravity anomalies. If such a correlation exists, it should be clearest in areas where the sense of displacement changes, as is predicted offshore West Africa.
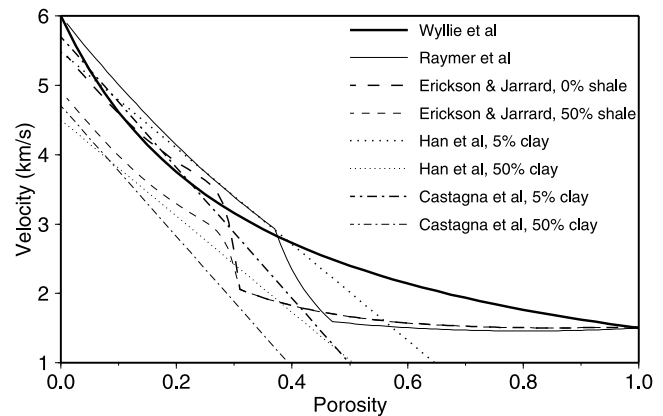
[10] An inverse model is developed to determine the magnitude of denudation that best fits V_{RMS} measurements obtained from individual common midpoint gathers (CMPs) during seismic reflection processing. By building a theoretical, one-dimensional, velocity profile and by minimizing the misfit between this synthetic profile and the observed profile, the amount of denudation can be constrained. We first consider the forward problem and later develop a practical inverse scheme which uses the simplest possible model which can adequately minimize misfit between theory and observation. As little a priori knowledge is assumed as possible in order to limit the number of unknown variables and to enable a good understanding of how uncertainty in model parameters maps into model space. Notation used is summarized in Table 1.

3. Forward Model

3.1. Velocity-Porosity Relationships

[11] The most commonly used model of seismic velocity, V, as a function of porosity, ϕ, is Wyllie's time-average equation [*Wyllie et al.*, 1956] which states that

$$\frac{1}{V} = \frac{\phi}{V_{fl}} + \frac{(1-\phi)}{V_{ma}} \qquad (1)$$

where V_{fl} and V_{ma} are the velocities of the pore fluid and rock matrix (Table 2). This empirical equation was

Table 3. Parameters of the Exponential Porosity-Depth Relation[a]

Lithology	ϕ_o	λ, km
Sand	0.5	2.5
Shale	0.6	2.0
Chalk	0.55	2.2
Basalt	0.1	2.5
Limestone	0.4	1.0
Dolostone	0.2	3.0
Anhydrite	0.4	0.5
Salt	0.2	0.75

[a]Values of parameters of the exponential porosity-depth relation (equation (5)) are determined by *Sclater and Christie* [1980] for North Sea lithologies.
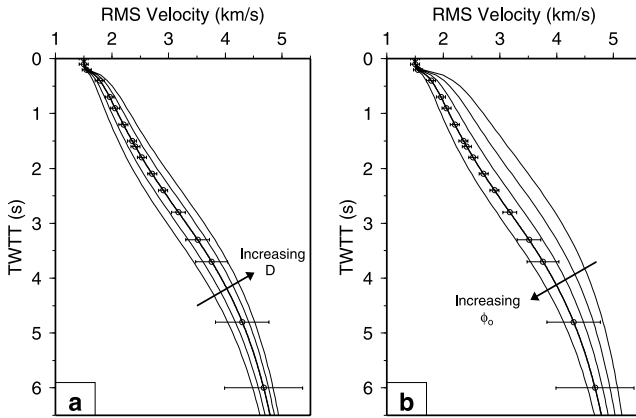
	Forward model	Inversion results	
		Unweighted	Weighted
D	0.45 km	-0.832	0.264
$\phi_\circ$	0.9	0.474	0.820
λ	2.0 km	2.000	2.000
V_{ma}	6.0 km s^{-1}	6.000	6.000
M		0.002	0.003

Figure 5. (a) Effect of varying D on modeled V_{RMS} curves. Data are synthetic, generated using forward model and discretized, with parameters D = 0.45 km, $\phi_\circ$ = 0.9, λ = 2 km, V_{ma} = 6 km s^{-1} and wd = 120 m. Curves represent forward models with D = 0.15, 0.3, 0.45, 0.6, 0.75 km. Bold curve represents result of inversion of synthetic data. Unweighted and weighted (W_1 = 10, W_2 = 1, W_3 = 50) models are coincident with D = 0.45 km forward model. (b) Effect of varying $\phi_\circ$ on modeled V_{RMS} curves. Data are as in Figure 5a. Curves represent forward models with $\phi_\circ$ = 0.6, 0.7, 0.8, 0.9, 1.0. Bold curve represents result of inversion of synthetic data, coincident with $\phi_\circ$ = 0.9 forward model.

constructed to describe velocities in sandstones with porosities of less than ∼30%. The *Wyllie et al.* [1956] equation was modified by *Raymer et al.* [1980] to describe the low (<2 km s^{-1}) and approximately constant velocities

observed in high-porosity sediments more accurately. In this case, velocity is given by

$$V = (1 - \phi)^2 V_{ma} + \phi V_{fl} \qquad \text{for } \phi < 0.37 \qquad (2)$$

$$\frac{1}{\rho V^2} = \frac{\phi}{\rho_{fl} V_{fl}^2} + \frac{1 - \phi}{\rho_{ma} V_{ma}^2} \qquad \text{for } \phi > 0.47 \qquad (3)$$

where ρ, ρ_{fl} and ρ_{ma} are the densities of the whole rock, the pore fluid and the rock matrix, respectively. For porosities between 37% and 47%, the velocity is determined by interpolation between V_{37}, the velocity at ϕ = 0.37 given by equation (2) and V_{47}, the velocity at ϕ = 0.47 given by equation (3):

$$\frac{1}{V} = \left(\frac{0.47 - \phi}{0.1}\right)\frac{1}{V_{37}} + \left(\frac{\phi - 0.37}{0.1}\right)\frac{1}{V_{47}} \qquad (4)$$

[12] Other authors have developed alternative velocity-porosity relationships (Figure 4). *Erickson and Jarrard* [1998] use a "critical porosity" at which velocity drops to a low, approximately constant value, in a similar manner to the curve of *Raymer et al.* [1980]. The majority of other relationships [e.g., *Castagna et al.*, 1985; *Han et al.*, 1986] are only valid for porosities less than ∼30%. Alternative velocity-porosity relationships were tested but they all generated significantly larger residual misfits compared to the Wyllie model.

3.2. Porosity-Depth Relationship

[13] We have exploited the widely used exponential porosity decay curve in which porosity is assumed to decrease exponentially with increasing depth, so that

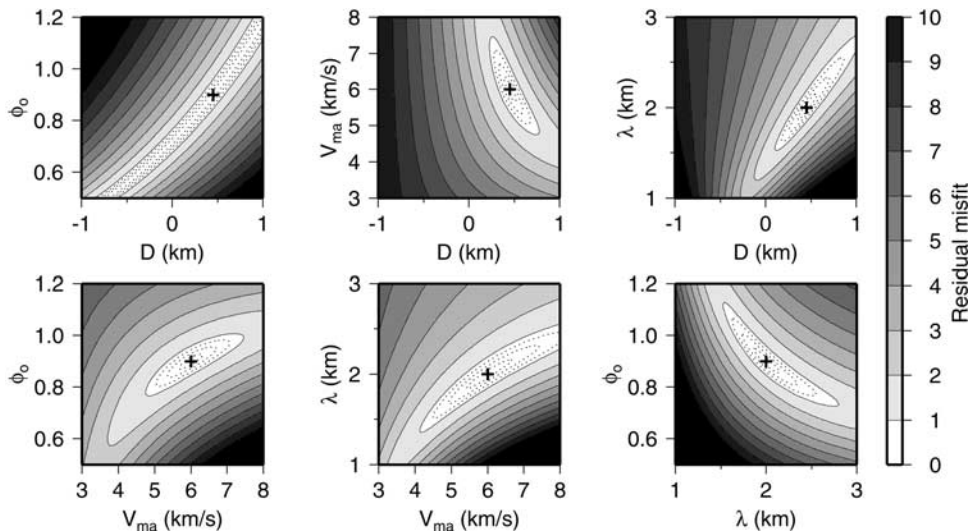$$\phi = \phi_\circ \exp[-(z - wd)/\lambda] \qquad (5)$$

Figure 6. Trade-off between the four inversion parameters for synthetic data with no weighting functions added to the misfit function (W_1 = 0, W_2 = 0). Crosses represent forward model parameters, as Figure 5. Dotted lines represent contour interval 0.25. Inner solid line corresponds to χ^2 of 1.
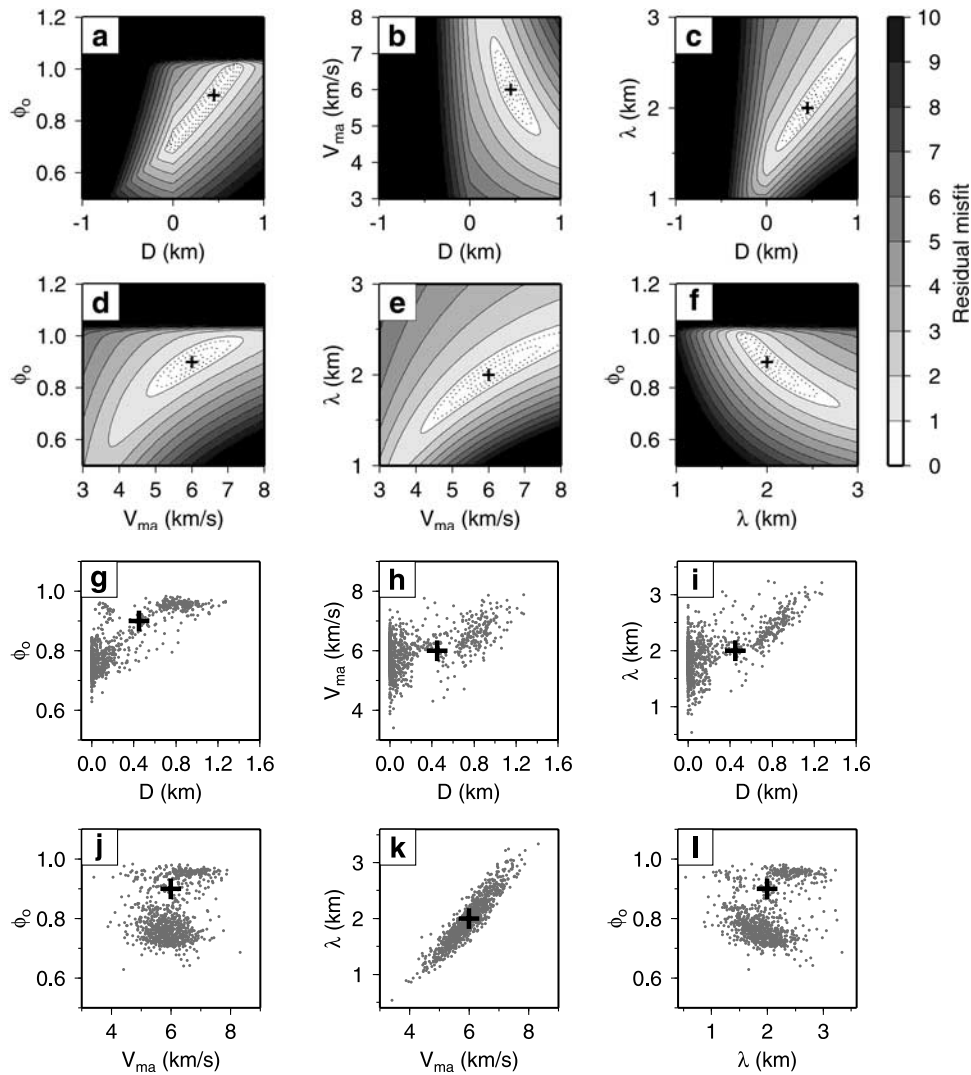
Figure 7. (a)–(f) Trade-off between the four inversion parameters for synthetic data with weighting functions added to the misfit function ($W_1 = 10$, $W_2 = 0.1$, $W_3 = 100$). Crosses represent forward model parameters, as Figure 5. Dotted lines represent contour interval 0.25. (g)–(l) Results of Monte Carlo modeling of synthetic data with random noise of ±0.1 s on TWTT and ±0.2 km s^{-1} on V_{RMS}. $W_1 = 10$ $W_2 = 0.1$ $W_3 = 100$. Crosses represent parameters of the synthetic forward model, as Figure 5. Starting solution for inversion is $\phi_\circ = 1.0$, $D = 0.0$ km, $V_{ma} = 4$ km s^{-1}, $\lambda = 0.5$ km.

where z is depth below sea level, wd is the water depth, $\phi_\circ$ is the initial porosity and λ is the porosity decay length. Values of $\phi_\circ$ and λ determined by *Sclater and Christie* [1980] for North Sea lithologies are given in Table 3. This approach is simplified and there is future scope in exploiting large amounts of local porosity depth information. Our justification is that Neogene strata offshore West Africa consist of a relatively simple combination of sand and shale.

[14] In the case of an uplifted and denuded section, the present-day depth does not necessarily represent maximum depth of burial. If strata have been eroded, depth is reduced and the porosity obtained from equation (5) will be anomalously high. Equation (5) must therefore be modified to take into account denudation, D, so that

$$\phi = \phi_\circ \exp[-(z - wd + D)/\lambda] \qquad (6)$$

Equation (6) can be combined with velocity-porosity relationships such as equation (1) or equations (2)–(4) in order to calculate velocity as a function of depth.

3.3. Conversion to RMS Velocity

[15] The velocity-porosity relationships described above use the seismic interval velocity, V_{int} (i.e., the velocity of a layer at a given depth). However, we wish to exploit V_{RMS} profiles. V_{RMS} is preferable since it represents the original velocity measurement generated during velocity analysis of prestack seismic data in order to correct for normal move out [*Yilmaz*, 2001]. In order to model V_{RMS}, we must convert synthetic interval velocity to RMS velocity. The two-way travel time, t, as a function of depth, z, is required when performing this conversion [*Yilmaz*, 2001]
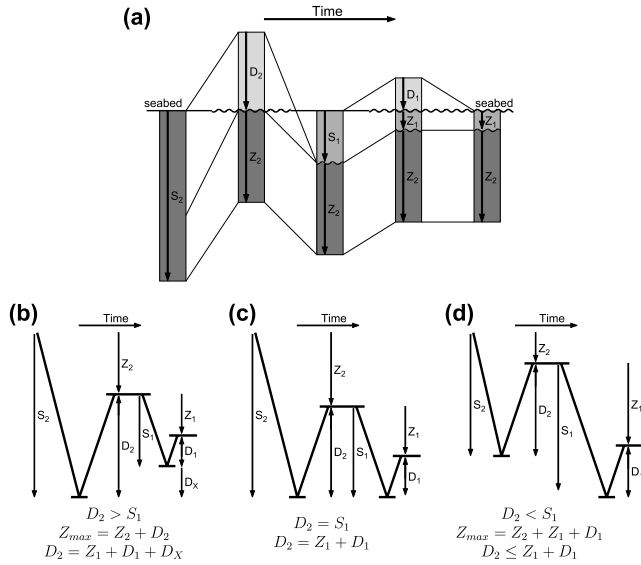
Figure 8. (a) Cartoon showing subsidence and denudation history of a stratigraphic column. (b)–(d) Cartoons showing the importance of the ratio of D_2 and S_1. If $D_2 \leq S_1$, then the maximum burial depth, $Z_{\max}$, during the first subsidence event, S_2, cannot be retrieved. An upper limit of $D_2 = S_1$ can be imposed.

$$t = 2 \int_0^z \frac{dz}{V_{\mathrm{int}}(z)}$$

V_{int} can now be expressed as a function of t rather than z. Once $V_{\mathrm{int}}(t)$ is known, V_{RMS} can be modeled as a function of t using

$$V_{\mathrm{RMS}}^2 = \frac{\int_0^t V_{\mathrm{int}}(t)^2 dt}{t}$$

This forward model generates V_{RMS} profiles that vary smoothly with t (Figure 5). The effect of denudation is to increase V_{RMS} at all depths below the seabed (Figure 5a). Velocity is also increased by decreasing $\phi_\circ$, indicative of trade-off between these two parameters. These forward models suggest that denudation can be resolved to within ± 150 m, as long as $\phi_\circ$ can be constrained to within ± 0.05. This uncertainty relationship is nearly linear as a function of depth.

4. Inverse Model

[16] The forward model can now be incorporated into an inversion algorithm which will search for a combination of values of D, $\phi_\circ$, λ and V_{ma} such that the misfit function, $M(D, \phi_\circ, \lambda, V_{ma})$, between the modeled V_{RMS} profile, V^c, and the measured V_{RMS} profile, V^o, as a function of two-way travel time is minimized (Figure 5). Minimization is achieved using Powell's algorithm [*Press et al.*, 1992]. $M(D, \phi_\circ, \lambda, V_{ma})$ is defined as

$$M = \sqrt{\frac{1}{n} \sum_{i=1}^n \left(\frac{V_i^o - V_i^c}{\sigma_i} \right)^2} + M_1 + W_2 e^{W_3(\phi_\circ - 1)} \quad (7)$$
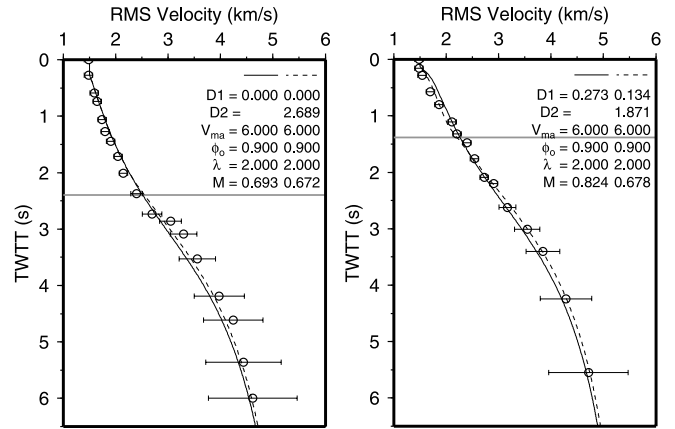

Figure 9. Examples of modeling with two levels of denudation. (a) Velocity profile 13, Figure 3. (b) Velocity profile 9, Figure 3. Gray line represents position of unconformity. Solid line represents inversion for D_1 only with no unconformity. Dashed line represents inversion for D_1 and D_2. In all cases, $W_1 = 10$.

where

$$M_1 = 0 \qquad \text{for } D \geq 0$$
$$M_1 = W_1(e^{-D} - 1) \qquad \text{for } D < 0$$

and n is the number of data points and σ is the error in observed V_{RMS}. W_1, W_2 and W_3 are weighting factors, typically equal to 10, 1, and 50, respectively. The first term on the right-hand side of equation (7) is the least squares misfit between V^o and V^c. This term is zero when calculated and observed values of V_{RMS} agree at all depths. The second term, M_1, applies weighting when $D < 0$, ensuring that D does not become negative, while the third term penalizes the misfit if the initial porosity, $\phi_\circ$, approaches 1. If $\phi_\circ > 1$, this term becomes very large. Weighting on D is not effective if the value of W_1 is 1. Values >10 give similar results to $W_1 = 10$. W_2 must be
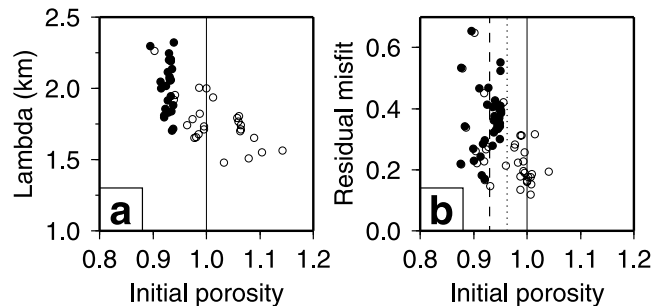

Figure 10. (a) The $\phi_\circ$ and λ results from inversion of deep-water velocity data with $D = 0$ and $V_{ma} = 6$ km s^{-1}. Open symbols represent unweighted models ($W_1 = 0$, $W_2 = 0$). Black symbols represent weighted models ($W_1 = 10$, $W_2 = 1$, $W_3 = 50$). (b) The $\phi_\circ$ results from inversion of deep-water velocity data with $D = 0$, $V_{ma} = 6$ km s^{-1} and $\lambda = 2$ km. Symbols are as in Figure 10a. Dotted line represents mean $\phi_\circ$ of unweighted models. Dashed line represents mean $\phi_\circ$ of weighted models.
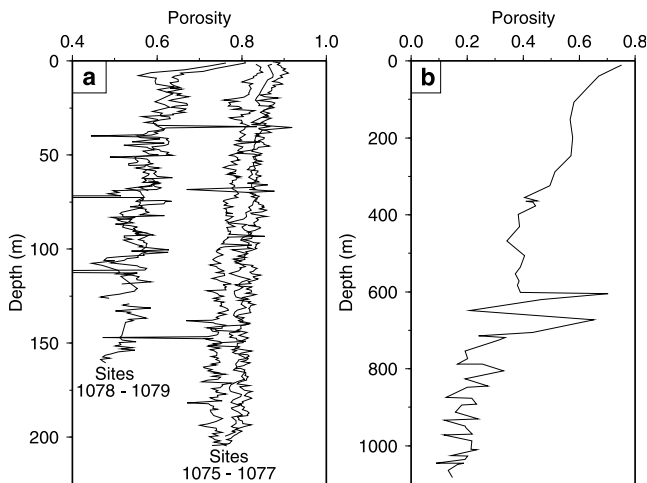
Figure 11. (a) Porosity-depth data from ODP Leg 175 [*Wefer et al.*, 2002]. (b) Porosity-depth data from DSDP site 364 [*Bolli et al.*, 1978]. See Figure 2 for site locations.

kept $\simeq 1$ to prevent significant weighting at $\phi < 0.8$, whereas W_3 is less sensitive and values of 20–70 have a relatively small effect on the wavelength of the weighting function.

[17] Input data for the inverse model consist of $t - V_{RMS}$ pairs from CMPs on seismic reflection profiles. Water depth at each CMP and the pore fluid velocity (1.5 km s^{-1}) are also supplied a priori. We have not included the effects of temperature, pressure and composition on this pore fluid velocity since these effects are relatively minor (e.g., the acoustic velocity of seawater at 10 MPa increases from 1.47 km s^{-1} to 1.51 km s^{-1} if temperature increases from 0°C to 100°C). If a velocity-porosity relation other than that of *Wyllie et al.* [1956] is used, the rock matrix and pore fluid densities and the shale or clay fraction may also be required. Error in t is assumed to be negligible whereas error in picked V_{RMS} increases with depth. A linear expression to describe the error in V_{RMS} was derived by inspecting synthetic NMO plots generated from information about acquisitional geometry. Approximately 100 estimates of the width of semblance peaks were used to define the error, σ, as

$$\sigma = 80 \text{ m s}^{-1} \qquad \text{for } t \leq 2565 \text{ ms} \qquad (8)$$

$$\sigma = 0.1767t - 373.26 \text{ m s}^{-1} \qquad \text{for } t > 2565 \text{ ms} \qquad (9)$$

Velocity picks in the topmost sedimentary rocks in shallow water are subject to error since refracted arrivals can obscure the first reflected arrivals and are often muted out, preventing accurate picking of NMO for near surface reflections. This imprecision can be a significant source of error in the top 500 ms in shallow water (water depth <1 s two-way travel time (TWTT)). However, since the V_{RMS} profile must increase smoothly between the seawater velocity at the seabed ($V_{fl} = 1.5 \pm 0.02$ km s^{-1}) and the well-constrained velocities in slightly deeper parts of the section, near-surface error is not significant.

[18] When W_1 and W_2 are set to zero, all four inversion parameters (D, $\phi_\circ$, λ and V_{ma}) are unconstrained. Denuda-

tion can be negative, the initial porosity can be >1 and the rock matrix velocity ranges from approximately 4–7 km s^{-1}. Trade-off between parameters for an unweighted inversion model of the synthetic data shown in Figure 5 are illustrated in Figure 6. In this synthetic case, V_{ma} and λ are successfully retrieved by the inversion. However, the significant trade-off between $\phi_\circ$ and D presents a problem (note locus of $\chi^2 = 1$ contour). Without a priori knowledge of the initial porosity of the sediment, we can clearly say little about the magnitude of denudation. The first thing to do is bound the problem to prevent nonphysical values occurring. Applying weighting functions to prevent D becoming negative or $\phi_\circ$ exceeding 1 modifies the trade-offs to those shown in Figures 7a–7f. The situation is improved but significant trade-off remains between D and $\phi_\circ$ (Figure 5). These two parameters cannot be retrieved successfully without additional a priori information.

[19] Bootstrap (i.e., Monte Carlo style) modeling was carried out on synthetic data to assess how errors in the data space map into errors in the solution space [*Press et al.*, 1992]. This approach provides a useful assessment of the distribution of errors in the estimated parameter set. In each test, 1000 inversions were performed with random noise added to the data in both t and V_{RMS} (±0.1 s on t, ±0.2 km s^{-1} on V_{RMS}). Results highlight the problem of trade-off between denudation and initial porosity (Figures 7g–7l). While porosity decay length and matrix velocity are retrieved with reasonable accuracy, denudation and initial porosity were not successfully constrained as there is no well-defined minimum in the residual misfit space (Figures 6 and 7a–7f). Clustering of $\phi_\circ$ and D results away from the known solution may indicate some degree of nonlinearity within the model space.

[20] Parameter trade-offs show similar trends for observed data as for synthetic data, with trade-off between D and $\phi_\circ$ causing most problems. Modeled denudation showed little, if any, correlation with the mapped extent of the major seabed unconformity (Figure 2). In fact, modeled denudation was close to zero over much of the area, an unsatisfactory result given the geometry of the stratigraphy observed (Figure 3). The other parameters ($\phi_\circ$, λ and V_{ma}) showed a good deal of variation across the region, also an unsatisfactory result. In a region where sedimentary facies change slowly, rock properties are expected to be broadly uniform. Any variation of rock properties is expected to be smooth, not showing the uneven distributions evident in inversion results.

Table 4. Best Fitting Compaction Parameters for ODP and DSDP Porosity-Depth Data[a]

Site	$\phi_\circ$	λ	Latitude	Longitude
		ODP 175		
1075	0.8697	1.8615	4.785°S	10.075°E
1076	0.8116	1.6485	5.069°S	11.102°E
1077	0.8495	2.1825	5.180°S	10.437°E
1078	0.6274	0.6749	11.920°S	13.400°E
1079	0.6838	0.3601	11.930°S	13.309°E
		DSDP		
364	0.7906	0.6685	11.572°S	11.972°E

[a]Values are for data shown in Figure 11. Locations of drilling sites are shown on Figure 2.
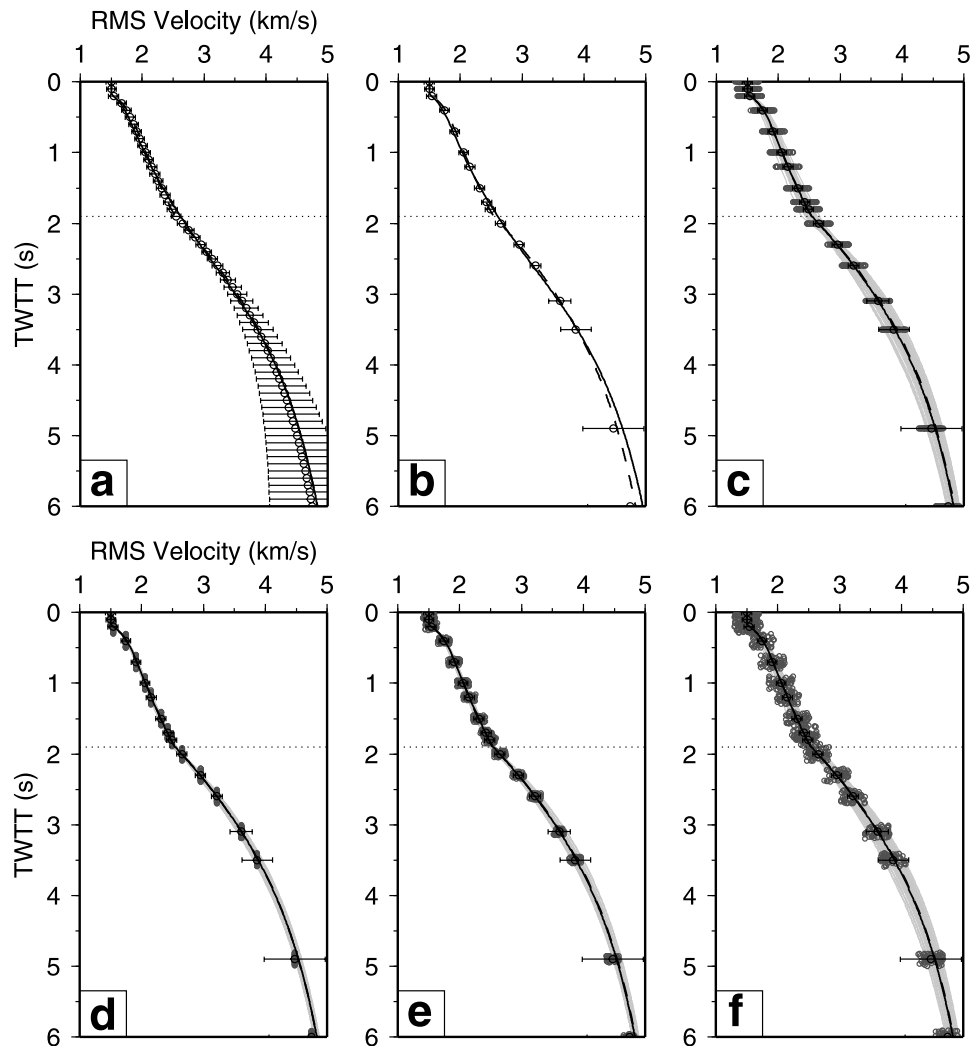
Figure 12. Synthetic tests on velocity inversion model. In all cases, $W_1 = 10$, $W_2 = 0$. Dotted line represents position of subsurface unconformity. (a) Uniform data distribution. Solid line represents all parameters free, one level of denudation (model 1, Table 5). Dashed line represents two levels of denudation, $V_{ma} = 6$ km s^{-1}, $\phi_o = 0.9$, $\lambda = 2$ km (model 2). (b) Same as Figure 12a but for discretized data (models 3 and 6). (c) Random noise of ± 0.2 km s^{-1} added to V_{RMS} (model 7). Fifty model runs are shown as gray lines. Solid line represents fit to data with no noise, $V_{ma} = 6$ km s^{-1}, $\phi_o = 0.9$, $\lambda = 2$ km (model 3). Dashed line represents forward model generated using mean denudation parameters for 50 noise runs. Two lines are coincident. (d) Same as Figure 12c but with random noise of ± 0.1 s added to TWTT (model 8). (e) Same as Figure 12c but with random noise of ± 0.1 km s^{-1} added to V_{RMS} and ± 0.05 s added to TWTT (model 9). (f) Same as Figure 12c but with random noise of ± 0.2 km s^{-1} added to V_{RMS} and ± 0.1 s added to TWTT (model 10).

[21] These initial test results suggest that ϕ_o should be independently constrained in order to model D. Adaptations to the modeling technique and independent information from the West African margin can been used to further constrain model parameters, thereby improving the reliability of modeling results. These strategies are described below.

5. A Bounded Inverse Model

5.1. Modeling Two Levels of Denudation

[22] Up to this point, the inverse model has been designed to account for one level of denudation, that at the seabed. However, it is quite apparent from the seismic data that there are two significant unconformities in the stratigraphy and it is not correct to assume just one episode of denudation: two unconformities must be included in the model. If the older unconformity is not incorporated, then the inversion is forced to fit the fast velocities of compacted rocks brought to shallow depths during Oligocene denudation by overestimating denudation at the surface. Modeled V_{RMS} are too fast just below the seabed and too slow below the Oligocene unconformity. Thus a robust estimate of seabed denudation cannot be achieved without taking the subsurface unconformity into account. This shortcoming of the model can be overcome by incorporating two levels of denudation in the inversion scheme. First, the section above the subsurface unconfor-

Table 5. Summary of Synthetic Test Results[a]

Model	n	N_V	N_t	D_1	D_2	V_{ma}	λ	ϕ_o
Forward model				0.370	3.450	5.82	1.85	0.917
1, V_{ma}, ϕ_o, λ, D	1	0	0	0.197	—	6.00	1.63	0.890
2, D_1, D_2	1	0	0	0.394	3.545	(6.00)	(2.00)	(0.900)
3, V_{ma}, ϕ_o, λ, D	1	0	0	0.255	—	6.22	1.70	0.915
4, D_1, D_2	1	0	0	0.370	3.448	(5.82)	(1.85)	(0.917)
5, D_1, D_2	50	0.2	0.1	0.364 ± 0.063	3.440 ± 0.434	(5.82)	(1.85)	(0.917)
6, D_1, D_2	1	0	0	0.397	3.557	(6.00)	(2.00)	(0.900)
7, D_1, D_2	50	0.2	0.0	0.392 ± 0.058	3.641 ± 0.359	(6.00)	(2.00)	(0.900)
8, D_1, D_2	50	0.0	0.1	0.396 ± 0.017	3.551 ± 0.138	(6.00)	(2.00)	(0.900)
9, D_1, D_2	50	0.1	0.05	0.387 ± 0.023	3.591 ± 0.097	(6.00)	(2.00)	(0.900)
10, D_1, D_2	50	0.2	0.1	0.396 ± 0.062	3.608 ± 0.358	(6.00)	(2.00)	(0.900)

[a]Models 1 and 2 used uniform data distribution. Models 3–10 used discretized synthetic data; n is number of runs, N_V is noise in V_{RMS}, and N_t is noise in TWTT. Numbers in parentheses are fixed in the model and therefore not inverted for. In all cases, $W_1 = 10$ and $W_2 = 0$. Several of the models are shown in Figure 12.

mity is inverted to obtain an estimate of denudation at the seabed. A model velocity profile is then constructed down to the level of the older unconformity, which remains unchanged, while deeper data are inverted to obtain the denudation at the second unconformity.

[23] However, this second inversion loop is not as simple as the first one. The denudation model is based on a porosity profile which relates the sediment porosity to the maximum depth of burial (equation (5)). In the case of a sedimentary section with two levels of denudation (Figure 8a), the maximum burial depth may have been achieved before the first denudation episode, D_2, or at some intermediate time between the two denudation events (Figures 8b–8d). In the latter case, the first maximum burial depth will have been overwritten by the second episode of subsidence, S_1, and only an upper limit of the magnitude of the first denudation event, D_2, can be constrained. If the first subsidence episode, S_2, generated the maximum burial, then an estimate can be made of the magnitude of D_2. The second inversion loop inverts for D_X and applies the same weighting function as for D: as in equation (7) the misfit, M, is severely penalized if $D_X < 0$. If the inversion returns a value of $D_X \leq 0$, then $S_1 \geq D_2$ and $Z_1 + D_1$ is an upper limit for D_2. However, if $D_X > 0$ then a value of D_2 can be calculated, since $D_2 = Z_1 + D_1 + D_X$ (Figure 8).

[24] Examples of modeling data using the inverse model with fixed parameters and two levels of denudation are shown in Figure 9. Residual misfit is reduced when the subsurface unconformity is taken into account.

5.2. Independent Parameter Information

5.2.1. Initial Porosity and Porosity Decay Length

[25] Oceanward of the continental shelf, where the water depth rapidly increases, the seabed unconformity dies out and no strata are missing from the top of the section (Figure 3). Data from the deep-water (depth >1 km) part of seismic profiles, where there is no denudation, were used to determine ϕ_o and λ by inverting the data for these parameters only. If D is set to zero and V_{ma} is fixed, the number of unknown parameters is reduced to just two. Fixing V_{ma} is reasonable since the velocity of the primary constituent (quartz) does not vary much. Nevertheless, we do carry out a series of tests where V_{ma} is varied.

[26] When the deep-water data are inverted to find ϕ_o and λ with no weighting functions applied there is significant scatter, reflecting the small trade-off between these two

parameters (Figures 6 and 10a). λ tends to lie in the range 1.5–2.0 km, while ϕ_o varies from 0.90 to 1.15. A value of λ toward the top end of this range (i.e., $\lambda \sim 2$ km) is favored as this value causes ϕ_o to be lower (i.e., <1) and, in the full inversion, D to be higher (>0 km; Figure 6). Adding weighting functions reduces the range of ϕ_o, and shifts λ to slightly higher values, typically 1.75–2.25 km. If λ is fixed at 2 km and the data are inverted for ϕ_o only, without weighting functions, the range of ϕ_o is reduced to ~ 0.9 (Figure 10b).

[27] Independent porosity-depth data sets are available from Ocean Drilling Program (ODP) and Deep Sea Drilling Project (DSDP) holes close to the seismic data area
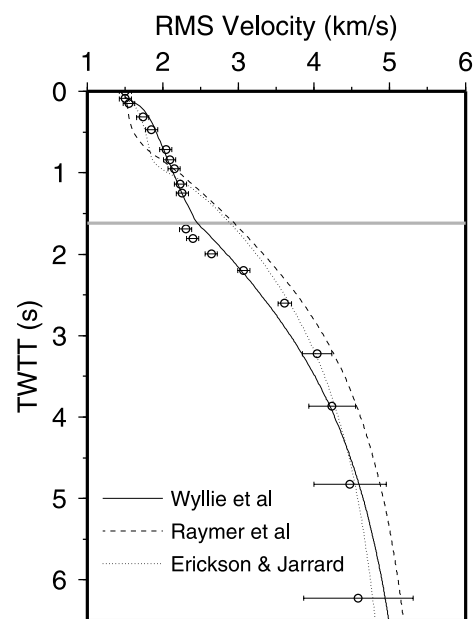
Model	D_1 (km)	D_2 (km)	Misfit
Wyllie et al	0.375	3.178	1.392
Raymer et al	1.089	3.178	4.124
Erickson & Jarrard	1.421	3.578	3.557

Figure 13. Results of inverse modeling using different velocity-porosity relationships for a velocity profile offshore Angola. Gray line = position of unconformity. In all models $V_{ma} = 6$ km s^{-1}, $\phi_o = 0.9$, $\lambda = 2$ km, $W_1 = 10$.
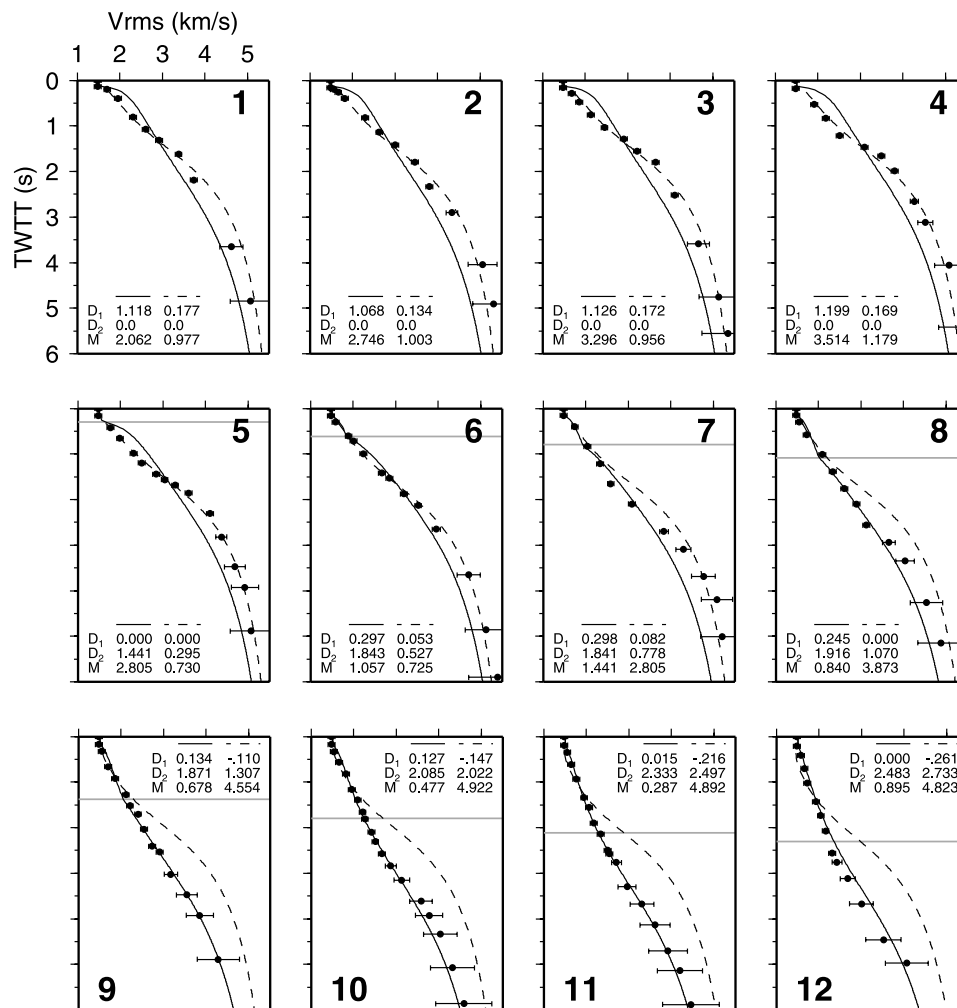
Figure 14. Inverse modeling results for velocity profiles 1–12 of Figure 3a. V_{ma} and ϕ_o fixed at 6 km s^{-1} and 0.9, respectively. Solid line represents λ fixed at 2 km. Dashed line represents λ fixed at 1 km. Gray represents position of subsurface (Oligocene) unconformity. Velocity profiles 1–4 are inshore of intersection of Oligocene unconformity with seabed, so have no value of D_2. Models with $\lambda = 1$ km fit these profiles better than models with $\lambda = 2$ km, suggesting that the Cretaceous-Paleogene section has properties different from the Neogene section.

(Figure 11) [*Wefer et al.*, 2002; *Bolli et al.*, 1978]. ODP Leg 175 included a group of three sites in the Lower Congo Basin offshore Congo, close to the test area (sites 1075– 1077) and two sites offshore Angola in the Kwanza Basin (sites 1078 and 1079), not far from the old DSDP site 364 (Figure 2). Surface porosity in all the Lower Congo Basin holes is surprisingly high (greater than ~0.85), lending strong support to inversion results that suggest high initial porosities. Porosity in the Kwanza Basin is lower although surface porosities of 0.7–0.8 are recorded in both ODP and DSDP holes. Values of ϕ_o and λ for each of the sites were determined by fitting exponential curves of the form of equation (5) to the data. Results are tabulated in Table 4. The only obvious anomaly concerns the measurements of λ which vary from 0.4 to 2.2 km. We emphasize that the newer ODP data from sites 1075– 1077 suggest that λ is 1.6–2.2 km in broad agreement with our results. If λ varies by ±500 m, the uncertainty in denudation is about ±200 m.

[28] Taking the results of inversion of velocity data in deep water and analysis of the ODP and DSDP data into account, the porosity parameters were fixed at $\phi_o = 0.9$ and $\lambda = 1.5$–2 km. Trade-off between ϕ_o and D means that uncertainty in ϕ_o of ±0.05 leads to error in D of ±150 m (Figure 5). It is important to note that the ODP porosity data suggest that there may be long-wavelength variation in ϕ_o and λ (Figure 11 and Table 4). Future implementations of the denudation algorithm could include regional porosity measurements.

5.2.2. Matrix Velocity

[29] The Cenozoic stratigraphy of the continental shelf is dominated by fine sandstones and mudstones [*Andersen et al.*, 2000]. The average rock matrix velocity is therefore predominantly influenced by the P wave velocity of quartz, 6.05 km s^{-1} (Table 2) [*Christensen*, 1982]. Other minerals that are likely to be present in the sediment, such as carbonates and salts, have velocities in the range 4.3 km s^{-1} to 6.6 km s^{-1}. In the constrained denudation
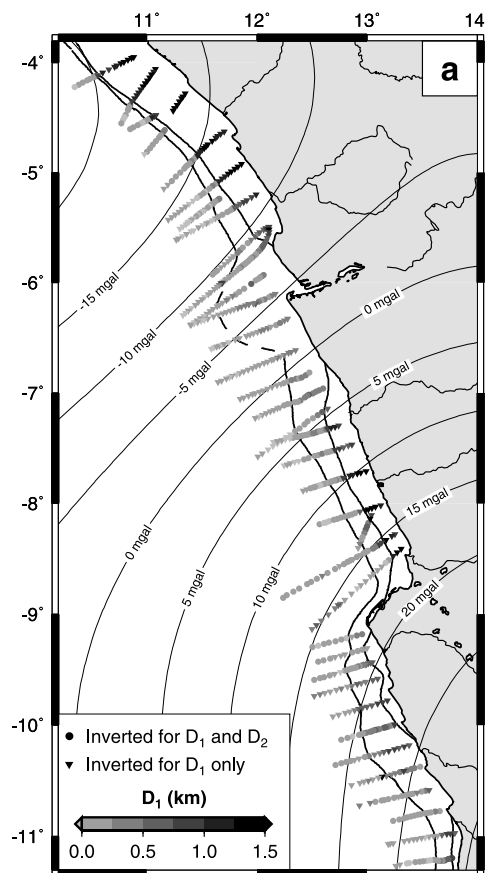
Figure 15. Maps of (a) D_1 results, (b) D_2 results, and (c) residual model misfit. Bold black lines represent seaward extent of seabed unconformity and intersection of Oligocene unconformity with seabed; Thin black lines represent 5 mGal contours of long-wavelength free-air gravity, equivalent to 100 m contours of dynamic topography when $Z = 50$ mGal km^{-1} (see text for details).

inversion model, V_{ma} is set at 6 km s^{-1}, which is close to the velocity of quartz.

[30] West African data were modeled with $\phi_\circ$ and λ fixed at 0.9 and 2 km, respectively, and V_{ma} set to 6 km s^{-1}, 6.5 km s^{-1} and 5 km s^{-1}, in order to take into account the range of possible matrix velocities. There was little difference between results with $V_{ma} = 6$ km s^{-1} and 6.5 km s^{-1}, whereas $V_{ma} = 5$ km s^{-1} caused denudation to be larger, sometimes unfeasibly large, and the model fit to be considerably poorer. By averaging the error at every CMP, which we defined to be one half of the range from D_{Vma5} to $D_{Vma6.5}$, an estimate of the uncertainty in denudation results was determined. At CMPs with only one unconformity (at the seabed), the uncertainty in D_1 is ±0.14 km. CMPs with no denudation ($D_1 < 0.001$ km) were not included in the calculation. At CMPs with two unconformities, uncertainty in D_1 is ±0.06 km and that in D_2 is ±0.7 km. In some cases, when $V_{ma} = 5$ km s^{-1} the model returned values of $D_2 > 10$ km. Such a large amount of denudation is regarded as unrealistic and these spurious results were removed from the uncertainty calculations since they skewed the result to much higher values.

5.3. Further Tests of the Inverse Model

[31] The behavior of the four parameter denudation inversion model and the modified, two layer inversion model with fixed velocity and compaction parameters were tested on synthetic data generated by a forward model. Synthetic data were initially generated with uniform spacing of data points in time (Figure 12a). Data were then decimated, leaving an uneven data distribution that better resembled real data (Figure 12b). Random noise was added to the synthetic data, in both time and velocity (Figures 12c–12f). The inversion model achieves a good fit to the data in all cases (Table 5). When V_{ma}, $\phi_\circ$ and λ are free and a second denudation level is not incorporated the model underestimates the denudation at the surface (model 3, Table 5). However, when V_{ma}, $\phi_\circ$ and λ are fixed, the inversion algorithm successfully retrieves both denudation parameters (D_1 and D_2; models 2, 4–10, Table 5).

[32] Wyllie's time-average equation (equation (1)) has been used in all modeling thus far, but alternative velocity-porosity relationships were also implemented in order to see if they resulted in improved fits. The formulae of equations (2)–(4) of *Raymer et al.* [1980] and *Erickson and Jarrard* [1998] were tested against that of *Wyllie et al.* [1956]. Neither of these alternatives improved the fit of inverse models (Figure 13). In fact, the fit was considerably poorer in both cases, due to the steep increase in velocity at porosities of ~0.3–0.4 which leads to a kink in the velocity profile at the depth corresponding to the 'critical porosity' (Figure 4). The data show no such rapid increase in V_{RMS} (the kink due to a subsurface unconformity is unrelated) and hence the formulae of *Raymer et al.* [1980] and *Erickson and Jarrard* [1998] result in large residual misfit. Consequently, Wyllie's time-average equation is used in all modeling.

6. Results

[33] V_{RMS} data from CDPs on dip lines offshore Congo and Angola have been modeled using the inversion model. $\phi_\circ$, λ and V_{ma} were held constant at 0.9, 2 km and 6 km s^{-1}, respectively. The model returns two denudation estimates: D_1 is denudation at the seabed and D_2 is denudation at the Oligocene unconformity.

[34] Inshore of the intersection of the Oligocene unconformity with the seabed, D_1 represents the combined denudation of the late Neogene and Oligocene unconformities. D_1 is correspondingly large (>1 km). However, residual misfit in this region is large (i.e., $M > 2$), probably because of the discrepancy between the porosity decay length used in the model ($\lambda = 2$ km) and the real value, which could be smaller (velocity profiles 1–4, Figure 14). A porosity decay length close to 1 km would be consistent with carbonate and evaporitic lithologies of the Cretaceous stratigraphy (Table 3). Setting $\lambda = 1$ km in the inversion significantly improves model fit ($M \simeq 1$) inshore of the intersection of the Oligocene unconformity with the seabed (Figure 14). However, these models have small D (<200 m), inconsistent with the erosional geometry observed (Figure 3). Alternative compaction parameters for the Cretaceous-Paleogene rocks have not been incorporated in fixed $\phi_\circ$ and λ models
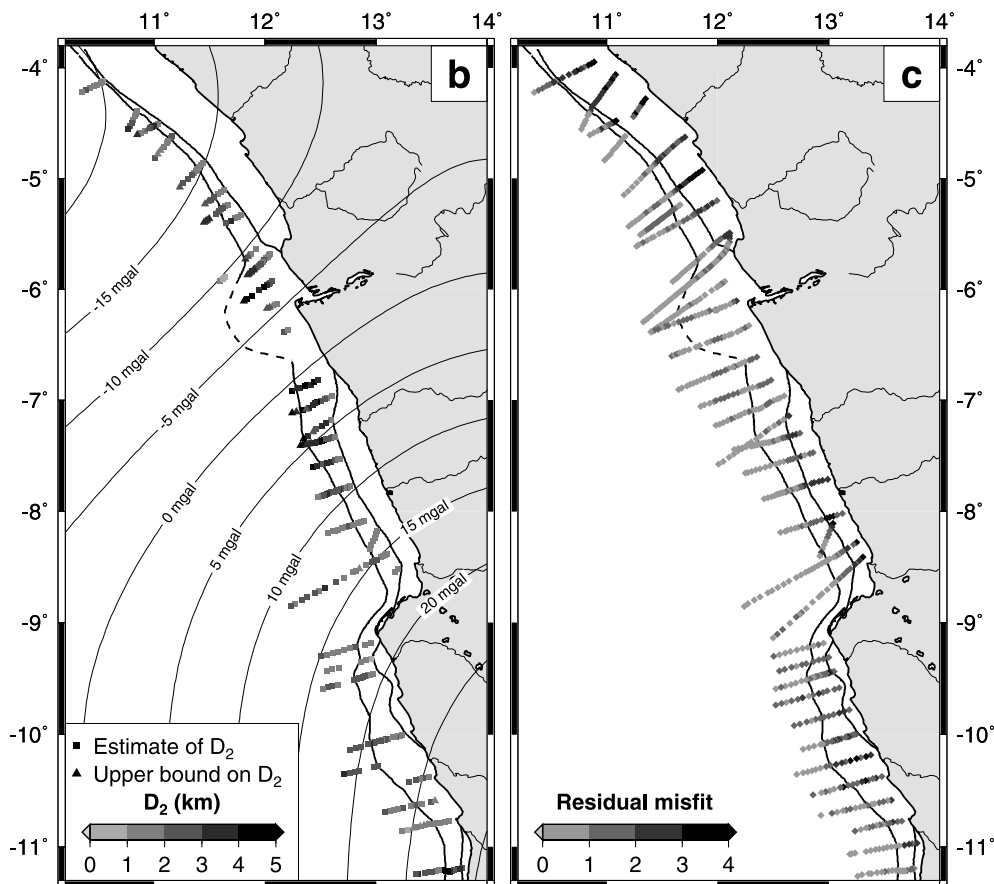
Figure 15. (continued)

due to lack of constraint and absence of independent estimates. A lower degree of confidence is attached to results in this region due to the poor model fit (Figure 15c).

[35] In the zone where both D_1 and D_2 are inverted for (i.e., oceanward of the intersection of the Oligocene unconformity with the seabed), D_1 exhibits some north-south variation (Figure 15a). In the north, where this zone is narrow, D_1 is typically ~300 m (Figures 3 and 14). In the vicinity of the Congo River mouth, D_1 is a little larger, typically 300 to 500 m, approximately twice the denudation estimated by *Cramez and Jackson* [2000] in the same region. *Walgenwitz et al.* [1990] estimated maximum denudation at around 7°S to be 900 m, whereas the largest values we calculate at similar locations are typically about 500 m. In the south, D_1 reaches values of 500 to 800 m (Figure 16). Seaward of the mapped extent of the seabed unconformity, the model returns values of $D_1 \simeq 0$, as is expected since no denudation is observed here on seismic reflection data (Figure 15a).

[36] In both the north and the south, denudation at the subsurface Oligocene unconformity (D_2) varies from ~0.5 km nearshore to ~2.5 km at the western ends of the lines (Figure 15b). The amplitude of the variation is in agreement with measurements of the minimum depth of incision on seismic data, which indicate denudation on the order of 1 km. Around the mouth of the Congo River, D_2 is as much as 5 km. It is difficult to assess whether this is a realistic value as the unconformity does not rise to the

seabed on the seismic reflection profiles, preventing a geometrical estimate from being made. Consistently high values of Oligocene denudation in the vicinity of the Congo River, typically 3–4 km, suggest that the behavior of the Congo River, and perhaps its interaction with ocean currents, was an important control on Oligocene denudation.

[37] There is a considerable thickness of Aptian salt (the Loeme Formation) along much of the west African shelf, deposited in the early stages of Atlantic breakup (Figure 3). The seismic velocity of salt is high since its low-porosity crystalline structure causes the bulk velocity to be dominated by the matrix velocity (Table 2). Where there is a significant thickness of salt, V_{RMS} becomes skewed toward fast velocities. Since the model assumes uniform lithology, it will compensate for fast velocity below the Oligocene unconformity by increasing D_2. Estimates of D_1 will be unaffected as they are only dependent upon velocities above the subsurface unconformity.

[38] Fortunately, the thickness of salt beneath much of the shelf is small, typically <15 m, and so will not significantly effect the V_{RMS} profile. However, large salt structures such as diapirs are observed in some areas offshore West Africa [e.g., *Duval et al.*, 1992; *Cramez and Jackson*, 2000; *Andersen et al.*, 2000; *Valle et al.*, 2001]. Additional uncertainty must be attached to estimates of D_2 in regions where the Aptian salt layer is thickened. Figure 16 shows that where the salt thickness exceeds ~0.2 s TWTT, D_2 results may be spurious.
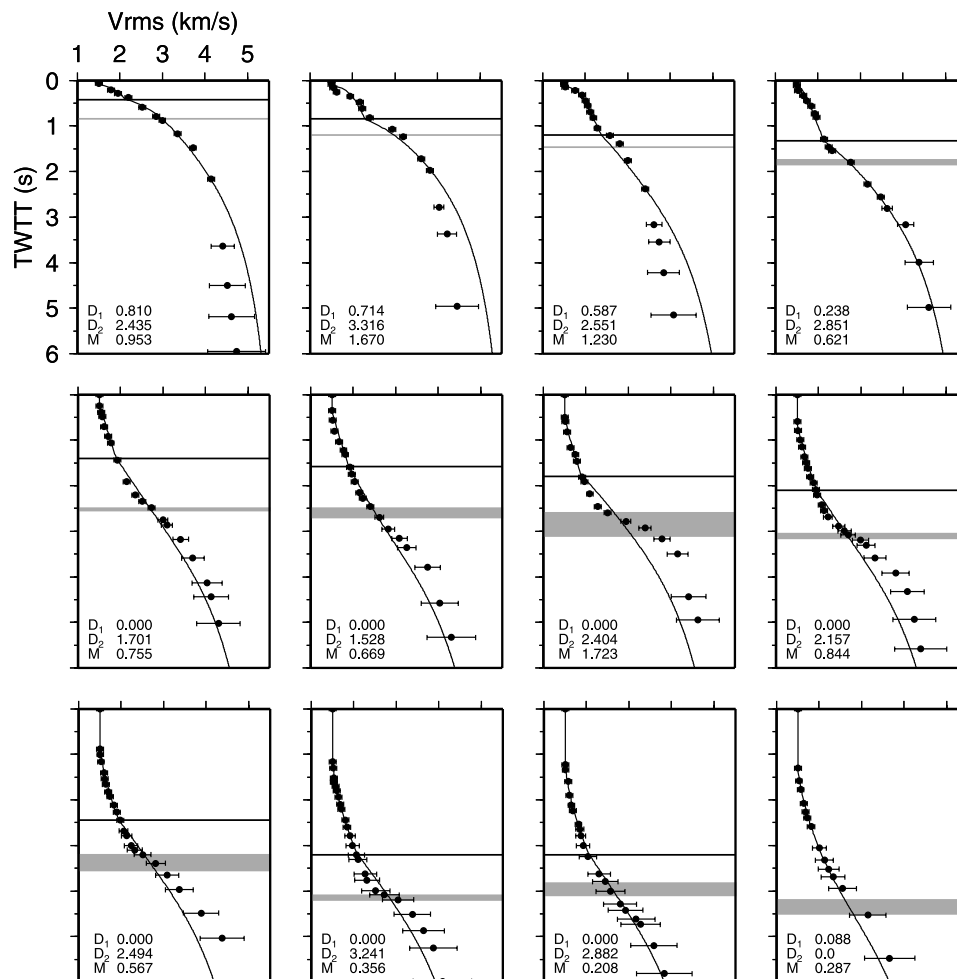
Figure 16. Inverse modeling results for a seismic profile offshore Angola. V_{ma}, ϕ_o and λ fixed at 6 km s^{-1}, 0.9 and 2 km, respectively. Black horizontal line represents position of subsurface (Oligocene) unconformity. Gray shading represents approximate position of salt. Note that below salt of significant thickness (>0.2 s TWTT) model underestimates $V_{\rm RMS}$.

6.1. Denudation and Dynamic Topography

[39] There is scope to improve this inverse model in the future. It would be useful to exploit porosity data from boreholes to define (or invert for) different compaction parameters above and below the Oligocene unconformity. The model gives a poor fit inshore of the intersection of the Oligocene unconformity with the seabed, where the Cretaceous Pinda limestone and Iabe salt dominate the shallow stratigraphy (Figures 14 and 15c). These lithologies have low values of λ and ϕ_o, very different to those of the clastic sequences that lie above them further offshore (Table 3). The model may perform better if different compaction parameters were used for pre-Oligocene lithologies.

[40] At present, the model first inverts for D_1, then holds it fixed while inverting for D_2. A better strategy may be to invert for the two denudation parameters simultaneously by searching for the combination of D_1 and D_2 that minimizes the misfit between the model and the data. It would be useful to model velocity data in parallel with other sources of denudation information, such as vitrinite reflectance and apatite fission track data sets, since a good denudation model should fit all of these constraints, subject to the limitations of the simple model used.

[41] In order to test the hypothesis that dynamic topography is the controlling influence on Neogene denudation, a region of West Africa with a steep long-wavelength gravity gradient was chosen for analysis (Figures 15a–15c). The long-wavelength gravity field has a minimum of −23 mGal at approximately 4°S offshore Gabon, rising to +28 mGal on the Angolan coast at 11°S.

[42] If mantle convection is driving vertical motions of the west African shelf and if long-wavelength gravity is a good proxy for the pattern of convection, there should be a correlation between the distribution and intensity of denudation and the long-wavelength gravity field. At present, the entire west African shelf is submarine but this submergence does not imply the existence of present-day dynamic subsidence since the Holocene marine transgression must be taken into account (~120 m).

[43] The largest denudation would be expected to occur in regions with a positive long-wavelength free-air gravity anomaly. In fact the opposite trend is observed (Figure 15a). Toward the south of the region investigated free-air gravity is positive and increasing, but the denudation is less than that observed north of the Congo River mouth where the gravity

anomaly is negative. These observations suggest that either the denudation is not controlled by dynamic topography, or that the long-wavelength gravity field is not a good proxy for the pattern of dynamic topography.

[44] The trend in late Neogene denudation, with the amount of denudation increasing toward the north, in consistent with the tomography-based prediction of dynamic topography of *Gurnis et al.* [2000] shown in Figure 1b. However, tomography-based models of dynamic topography are highly variable, being dependent not only on the tomographic model used, but also on the assumed mantle rheology. The dynamic topography prediction of *Lithgow-Bertelloni and Silver* [1998], using the tomography of *Grand et al.* [1997], shows a decrease from Angola to Gabon, the opposite trend to Figure 1b. Other models of *Gurnis et al.* [2000] using different rheologies to Figure 1b, and the model of *Conrad and Gurnis* [2003] have approximately constant values of dynamic topography along the stretch of west African shelf considered here. In future, maps of denudation calculated using our new inverse model could be used in tomography-based modeling to place important constraints on the rheological properties of the mantle, in particular its viscosity structure.

References

Andersen, J. E., J. Cartwright, S. J. Drysdall, and N. Vivian (2000), Controls on turbidite sand deposition during gravity-driven extension of a passive margin: Examples from Miocene sediments in Block 4, Angola, *Mar. Pet. Geol.*, *17*, 1165–1203.

Bolli, H. M., W. B. F. Ryan, and Shipboard Scientific Party (1978), Angola continental margin—Sites 364 and 365, *Initial Rep. Deep Sea Drill. Proj.*, *40*, 357–456.

Bond, G. (1978), Evidence for Late Tertiary uplift of Africa relative to North America, South America, Australia and Europe, *Tectonophysics*, *94*, 205–222.

Brice, S. E., M. D. Cochran, G. Pardo, and A. D. Edwards (1982), Tectonics and sedimentation of the South Atlantic rift sequence: Cabinda, Angola, in *Studies in Continental Margin Geology*, edited by J. S. Watkins and C. L. Drake, *AAPG Mem.*, *34*, 5–18.

Brown, R. W., D. J. Rust, M. A. Summerfield, A. J. W. Gleadow, and M. C. J. de Wit (1990), An early Cretaceous phase of accelerated erosion on the south-western margin of Africa: Evidence from apatite fission track analysis and the offshore sedimentary record, *Nucl. Tracks Radiat. Measur.*, *17*, 339–350.

Burke, K. (1996), The African plate, *S. Afr. J. Geol.*, *99*, 341–409.

Castagna, J. P., M. L. Batzle, and R. L. Eastwood (1985), Relationships between compressional-wave and shear-wave velocities in clastic silicate rocks, *Geophysics*, *50*, 571–581.

Christensen, N. I. (1982), Seismic velocities, in *Handbook of physical properties of rocks*, vol. II, edited by R. S. Carmichael, pp. 57–74, CRC Press, Boca Raton, Fla.

Cogley, J. G. (1985), Hypsometry of the continents, *Z. Geomorphol.*, *53*, 1–48.

Conrad, C. P., and M. Gurnis (2003), Seismic tomography, surface uplift, and the breakup of Gondwanaland: Integrating mantle convection backwards in time, *Geochem. Geophys. Geosyst.*, *4*(3), 1031, doi:10.1029/2001GC000299.

Cramez, C., and M. P. A. Jackson (2000), Superposed deformation straddling the continental-oceanic transition in deep-water Angola, *Mar. Pet. Geol.*, *17*, 1095–1109.

Duval, B., C. Cramez, and M. P. A. Jackson (1992), Raft tectonics in the Kwanza Basin, Angola, *Mar. Pet. Geol.*, *9*, 389–404.

Erickson, S. N., and R. D. Jarrard (1998), Velocity-porosity relationships for water-saturated siliciclastic sediments, *J. Geophys. Res.*, *103*, 30,385–30,406.

Gosse, J. C., and F. M. Phillips (2001), Terrestrial in situ cosmogenic nuclides: Theory and application, *Quat. Sci. Rev.*, *20*, 1475–1560.

Grand, S. P., R. D. van der Hilst, and S. Widiyantoro (1997), Global seismic tomography: A snapshot of convection in the Earth, *GSA Today*, *7*, 1–7.

Gurnis, M., J. X. Mitrovica, J. Ritsema, and H.-J. van Heijst (2000), Constraining mantle density structure using geological evidence of surface uplift rates: The case of the African Superplume, *Geochem. Geophys. Geosyst.*, *1*, doi:10.1029/1999GC000035.

Han, D., A. Nur, and D. Morgan (1986), Effects of porosity and clay content on wave velocities in sandstones, *Geophysics*, *51*, 2093–2107.

Hillis, R. R. (1992), Evidence of Pliocene erosion at Ashmore Reef (Timor Sea) from the sonic velocities of Neogene limestone formations, *Explor. Geophys.*, *23*, 489–495.

Hillis, R. R. (1995), Quantification of Tertiary exhumation in the United Kingdom southern North Sea using sonic velocity data, *AAPG Bull.*, *79*, 130–152.

Holmes, A. (1965), *Principles of Physical Geology*, 2nd ed., Nelson, London.

Jones, S. M., N. J. White, and B. Lovell (2001), Cenozoic and Cretaceous transient uplift in the Porcupine Basin and its relationship to a mantle plume, in *The Petroleum Exploration of Ireland's Offshore Basins*, edited by P. M. Shannon, P. D. W. Haughton, and D. V. Corcoran, *Geol. Soc. Spec. Publ.*, *188*, 345–360.

Karner, G. D., N. W. Driscoll, J. P. McGinnis, W. D. Brumbaugh, and N. R. Cameron (1997), Tectonic significance of the syn-rift sediment packages across the Gabon-Cabinda continental margin, *Mar. Pet. Geol.*, *14*, 973–1000.

Lithgow-Bertelloni, C., and P. G. Silver (1998), Dynamic topography, plate driving forces and the African superswell, *Nature*, *395*, 269–272.

Mavko, G., T. Mukerji, and J. Dvorkin (1998), *The Rock Physics Handbook: Tools for Seismic Analysis in Porous Media*, Cambridge Univ. Press, New York.

McKenzie, D. (1994), The relationship between topography and gravity on Earth and Venus, *Icarus*, *112*, 55–88.

Nyblade, A. A., and S. W. Robinson (1994), The African Superswell, *Geophys. Res. Lett.*, *21*, 765–768.

Parsons, B., and S. Daly (1983), The relationship between surface topography, gravity anomalies, and temperature structure of convection, *J. Geophys. Res.*, *88*, 1129–1144.

Partridge, T. C. (1998), Of diamonds, dinosaurs and diastrophism: 150 million years of landscape evolution in southern Africa, *S. Afr. J. Geol.*, *101*, 167–184.

Press, W. H., S. A. Teukolsky, W. T. Vettering, and B. P. Flannery (1992), *Numerical Recipes in FORTRAN: The Art of Scientific Computing*, 2nd ed., Cambridge Univ. Press, New York.

Raymer, L. L., E. R. Hunt, and J. S. Gardner (1980), An improved sonic transit time-to-porosity transform, *Trans. SPWLA Annu. Logging Symp.*, *21*, P1–P13.

Ritsema, J., H. J. van Heijst, and J. H. Woodhouse (1999), Complex shear wave velocity structure imaged beneath Africa and Iceland, *Science*, *286*, 1925–1928.

Rowley, E. J., and N. J. White (1998), Inverse modelling of extension and denudation in the East Irish Sea and surrounding areas, *Earth Planet. Sci. Lett.*, *161*, 57–71.

Sclater, J. G., and P. A. F. Christie (1980), Continental stretching: An explanation of the post-mid-Cretaceous subsidence of the central North Sea basin, *J. Geophys. Res.*, *85*, 3711–3739.

Sclater, J. G., L. A. Lawver, and B. Parsons (1975), Comparison of long wavelength residual elevation and free-air gravity anomalies in the North Atlantic and possible implications for the thickness of the lithospheric plate, *J. Geophys. Res.*, *80*, 1031–1052.

Séranne, M. (1999), Early Oligocene stratigraphic turnover on the west Africa continental margin: A signature of the Tertiary greenhouse-to-icehouse transition?, *Terra Nova*, *11*, 135–140.

Séranne, M., M. Seguret, and M. Fauchier (1992), Seismic super-units and post-rift evolution of the continental passive margin of southern Gabon, *Bull. Soc. Geol. Fr.*, *163*, 135–146.

Teisserenc, P., and J. Villemin (1990), Sedimentary basin of Gabon—Geology and oil systems, in *Divergent/Passive Margin Basins*, edited by J. D. Edwards and P. A. Santogrossi, *AAPG Mem.*, *48*, 117–199.

Uenzelmann-Neben, G. (1998), Neogene sedimentation history of the Congo Fan, *Mar. Pet. Geol.*, *15*, 635–650.

Uenzelmann-Neben, G., V. Speiss, and U. Bleil (1997), A seismic reconnaisance survey of the northen Congo Fan, *Mar. Pet. Geol.*, *140*, 283–306.

Valle, P. J., J. G. Gjelberg, and W. Helland-Hansen (2001), Tectonostratigraphic development in the eastern Lower Congo Basin offshore Angola, West Africa, *Mar. Pet. Geol.*, *18*, 909–927.

Vance, D., M. Bickle, S. Ivy-Ochs, and P. W. Kubik (2003), Erosion and exhumation in the Himalaya from cosmogenic isotope inventories of river sediments, *Earth Planet. Sci. Lett.*, *206*, 273–288.

van der Hilst, R. D., S. Widiyantoro, and E. R. Engdahl (1997), Evidence for deep mantle circulation from global tomography, *Nature*, *386*, 578–584.

Walgenwitz, F., M. Pagel, A. Meyer, H. Maluski, and P. Moine (1990), Thermo-chronological approach to reservoir diagensis in the offshore Angola basin: A fluid inclusion, ^{40}Ar-^{39}Ar and K-Ar investigation, *AAPG Bull.*, *74*, 547–563.

Ware, P. D., and J. P. Turner (2002), Sonic velocity analysis of the Tertiary denudation of the Irish Sea basin, in *Exhumation of the North Atlantic Margin; Timing, Mechanisms and Implications for Petroleum Exploration*, edited by A. G. Doré et al., *Geol. Soc. Spec. Publ.*, *196*, 355–370.

Wefer, G., W. H. Berger, and Shipboard Scientific Party (2002), *Proceedings of the Ocean Drilling Program, Initial Reports*, vol. 175, Ocean Drill. Program, College Station, Tex.

Wessel, P., and W. H. F. Smith (1998), New, improved version of Generic Mapping Tools released, *Eos Trans. AGU*, *79*, 579.

Wheeler, P., and N. J. White (2000), Quest for dynamic topography: Observations from Southeast Asia, *Geology*, *28*, 963–966.

Wyllie, M. R. J., J. A. R. Gregory, and L. W. Gardner (1956), Elastic wave properties in heterogeneous and porous media, *Geophysics*, *21*, 41–70.

Yilmaz, Ö. (2001), Seismic data analysis: Processing, inversion and interpretation of seismic data, *Invest. Geophys. 10*, Soc. of Explor. Geophys., Tulsa, Okla.

Zhao, D. (2001), Seismic structure and origin of hotspots and mantle plumes, *Earth Planet. Sci. Lett.*, *192*, 251–265.

————————————

H. L. Walford and N. J. White, Bullard Laboratories, Department of Earth Sciences, University of Cambridge, Madingley Rise, Madingley Road, Cambridge CB3 0EZ, UK. (nwhite@esc.cam.ac.uk)